

Supplementary Materials for

Electrostatic footpads enable agile insect-scale soft robots with trajectory control

Jiaming Liang *et al.*

Corresponding author: Min Zhang, zhang.min@sz.tsinghua.edu.cn (M.Z.); Junwen Zhong, junwenzhong@um.edu.mo (J.Z.);
Liwei Lin, lwlin@berkeley.edu (L.L.)

Published 30 June 2021, *Sci. Robot.* **6**, eabe7906 (2021)
DOI: 10.1126/scirobot.abe7906

The PDF file includes:

Sections S1 to S9
Figs. S1 to S16
Tables S1 to S4
References (57, 58)

Other Supplementary Material for this manuscript includes the following:

Movies S1 to S16

List of symbols and abbreviations

BL	body length
CG	center of gravity
f	friction force
R_{body}	body curvature radius
F_{iN}	normal force of each point i
Leg_z	leg height
Arc_h	body arch height
Arc_l	half of the body length
f_{act}	equivalent driving force of the actuator
pe	conversion coefficient
x, y, z	positions of center of gravity
$\dot{x}, \dot{y}, \dot{z}$	velocities of center of gravity
$\ddot{x}, \ddot{y}, \ddot{z}$	accelerations of center of gravity
$foot_z$	foot height
kb	spring coefficient of the robot body
db	damping coefficient of the robot body
\bar{v}_i	velocity vector in global coordinate system, subscript i denotes the point number
v_{cg}	velocity of center of gravity in global coordinate system
$r_{i,j}$	point position in local coordinate system, subscript i denotes the point number, j denotes the component, $j = 1, x$ component, $j = 2, y$ component
g	gravitational acceleration
φ	structure angle of the front foot
β	structure angle of the front leg
C_{tf}	length from the CG to the front foot
r_{rear}	structure parameter to define the rear leg position
f_s	reaction force on CG
$bias$	bias voltage
μ_d	coefficient of dynamic friction
μ_s	coefficient of static friction
v_r	relative speed
v_s	coefficient of sliding speed
p	exponent
k_t	slope adjustment parameter
d	thickness of the pad
μ_0	coefficient of dynamic friction with no bias
A	contact area
ϵ_0	vacuum permittivity
ϵ_r	relative permittivity
F_g	gravitational force
d	thickness of the dielectric layer
V_{pp}	peak to peak voltage applies on PVDF
θ	rotation angle in global coordinate

$u(t)$	robot driving signal
$freq$	frequency of driving signals
t	time
ω	angular velocity of center of gravity
\bar{f}_i	friction vector in global coordinate, i denotes the point number
\bar{f}'_i	friction vector in local coordinate, i denotes the point number
f_{iN}	normal force in global coordinate, i denotes the point number
\bar{r}_i	point position vector in local coordinate
T	torque
f'_{ij}	friction component in local coordinate, subscript i denotes the point number, j denotes the component, $j = 1, x$ component, $j = 2, y$ component
m	mass of the robot
I_{cm}	moment of inertia of center of gravity
COT	cost of transport

Section 1: Actuation mechanism of PVDF film and curved unimorph structure

The actuation mechanism of the main body (18) is shown in **Fig. S1**. When the externally applied electric field is in the opposite direction of the original polarization direction of the PVDF film, the PVDF film extends in the horizontal direction. In contrast, if the applied electric field is in the same direction of the original polarization direction, the material contracts (**Fig. S1A**). When PVDF and PET are laminated together as a unimorph curved structure, the structural curvature changes as the voltage varies, while the PET film does not change its length under the applied voltage. The radius R_0 (under 0 V) decreases to R_- if the applied electrical field is in the opposite direction as the original polarization direction of the PVDF film and increases to R_+ if the applied electrical field is in the same direction as the original polarization direction of the PVDF film (**Fig. S1B**).

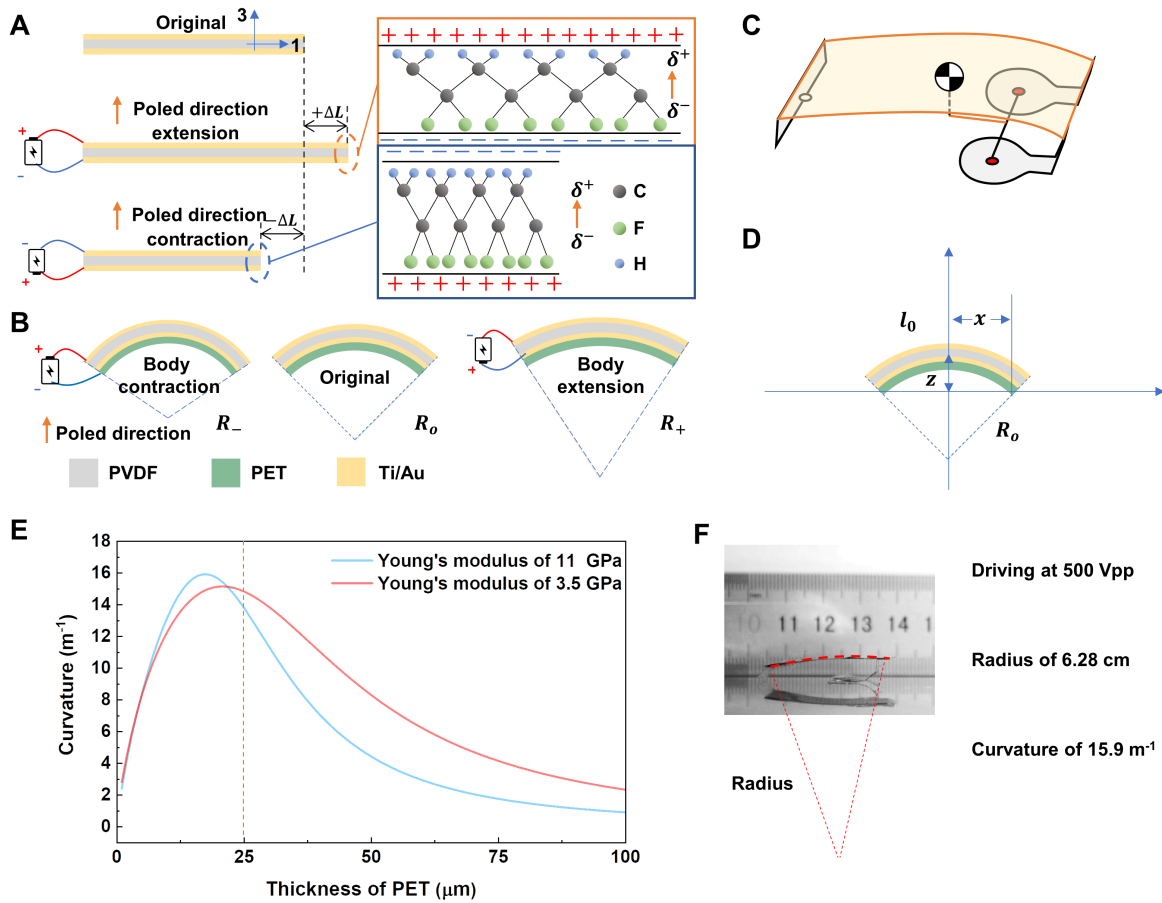


Fig. S1. The driving principle of the robot main body. **(A)** Piezoelectric effects of a poled PVDF film under electrical fields. **(B)** The curvature of the unimorph structure under positive, zero, and negative electrical fields. **(C)** The simplified model of the robot. **(D)** Definition of various parameters. **(E)** The relationship between the curvature of the main body structure and the thickness of the PET layer. **(F)** The bending of the

main body during the locomotion under the 500 Vpp driving voltage.

The assembled robot (**Fig. S1C**) and the variations of the radius (**Fig. S1D**) of the curved robot body can be approximately estimated, as shown in **Fig. S1E** (57). The specific experimental values of various materials used in this work are listed in **Table S1**. Specifically, the parameters t_1 , t_2 , and t_3 are the thickness and E_1 , E_2 , and E_3 are the biaxial Young's modulus of the PVDF film, silicone adhesive, and the PET films, respectively. By using U as the applied AC driving voltage and d_{31} as the piezoelectric constant, the strain in the PVDF film, ϵ , can be estimated based on the piezoelectric effect. The radius of curvature, R_{body} , is dependent on solutions of three parameters: ϵ , c , and t_b , by Eqs. (1), (2) and (3) as derived as in ref. (57):

$$\epsilon = \frac{Ud_{31}}{t_1} \quad (1)$$

$$c = \frac{E_1 t_1 \epsilon}{E_3 t_3 + E_2 t_2 + E_1 t_1} \quad (2)$$

$$t_b = \frac{-E_3 t_3^2 + E_2 t_2^2 + E_1 t_1 (2t_2 + t_1)}{2(E_3 t_3 + E_2 t_2 + E_1 t_1)} \quad (3)$$

$$\frac{1}{R_{\text{body}}} = \frac{3[ct_3^2(E_3 - E_2) - E_1 t_1(c - \epsilon)(2t_2 + t_1)]}{E_3 t_3^2(2t_3 + 3t_b) + E_2 t_2(2t_2^2 - 3t_2 t_b) + E_1 t_1(6t_2^2 + 6t_1 t_2 - 6t_2 t_b + 2t_1^2 - 3t_1 t_b)} \quad (4)$$

If the original radius of curvature (before applying the external voltage) of the robot body is infinity, **Fig S1E** shows the theoretical new radius of curvature versus the thicknesses of the PET film under a 500 V voltage. It is found the maximum curvatures will reach 16 m^{-1} and 15 m^{-1} by using a 17 μm -thick and 21 μm -thick PET films corresponding to Young's modulus of PET at 11 and 3.5 Gpa, respectively. In order to construct the robot's main body with the maximum bending motion, the optimal thickness of the PET film is between 17 to 21 μm . However, the thinnest PET available from the vendor (Gizmo Dorks) is 25 μm and it is chosen in this work. Furthermore, the PET film comes with another 25 μm -thick silicone as the adhesive layer, which is very soft to have little impact on the curvature of the body. **Fig. S1F** shows the experimental results for the bending of the main robot body during locomotion under a driving voltage of 500 Vpp, and the maximum curvature is measured as 15.9 m^{-1} , which falls within the range of the theoretical estimations.

Table S1. Material parameters

	PVDF	Silicone adhesive	PET
Thickness	$t_1 = 18 \mu\text{m}$	$t_2 = 25 \mu\text{m}$	$t_3 = 25 \mu\text{m}$
Width	$w_1 = 15 \text{ mm}$	$w_2 = 15 \text{ mm}$	$w_3 = 15 \text{ mm}$
Young's modulus	$E_1 = 2.8 \sim 3.2 \text{ GPa}$	$E_2 = 1 \sim 50 \text{ MPa}$	$E_3 = 3.5 \sim 11 \text{ GPa}$
Density	$\rho_1 = 1.78 \text{ g/cm}^3$	$\rho_2 = 1.2 \text{ g/cm}^3$	$\rho_3 = 1.38 \text{ g/cm}^3$
Piezo strain constant	$d_{31} = 30 \text{ pC/N}$	—	—
Piezo stress constant	$g_{31} = 0.21 \text{ Vm/N}$	—	—
Relative permittivity	$\epsilon_{r1} = 12.83$	$\epsilon_{r2} = 3.3$	$\epsilon_{r3} = 3.7$
Poison ratio	$\nu_1 = 0.34 \sim 0.39$	$\nu_2 = 0.47 \sim 0.49$	$\nu_3 = 0.37 \sim 0.44$

Section 2: Friction force measurement

Measuring friction force between PI films and ground substrates of paper (printer paper 80 g/m² No. 7378, Deli Inc.), polymer (frosted Polyvinyl chloride - PVC, Foojo Inc.), and metal (InSnBi alloy-DG47, DingGuan Inc.): A 2×2 cm² PI film with 10 nm-thick Ti/100 nm-thick Au films as the electrode is used as the testing material and the experimental setup is shown in **Fig. S2A**. A flat mass scale of 1.72 grams in weight is placed on top of the testing film to flatten the contact area on top of a flat glass plate. The testing film is connected with a 50 μm in diameter silver wire, which runs through two ultra-smooth micro zirconia pulleys (695CE, XUNDAZC) mounted on a small 3D-printed ABS holder to transmit the applied force along the axis of the force gauge (Series 7, MARK-10). The force gauge is mounted on a vertical linear translation stage (DDSM50, Thorlabs). The footpad electrodes are connected to the amplifier (ATA-2082, Agitek), and a waveform generator (DG 1062Z, RIGOL) is used to generate the applied voltages. After measuring the friction forces, one can obtain the friction coefficients for PI film with respect to various substrates, as shown in **Fig. S2B**. The roughness of the three testing surfaces is measured through a surface profiler (P-7 stylus profiler, KLA-Tencor) in **Figs. S2C-2E**. The polymer substrate has the largest surface roughness with R_a of 94.90 μm; the metal substrate has the medium surface roughness with R_a of 52.05 μm; and the paper has the lowest surface roughness with R_a of 15.75 μm. Thus, the friction coefficient between polymer and PI has the largest value.

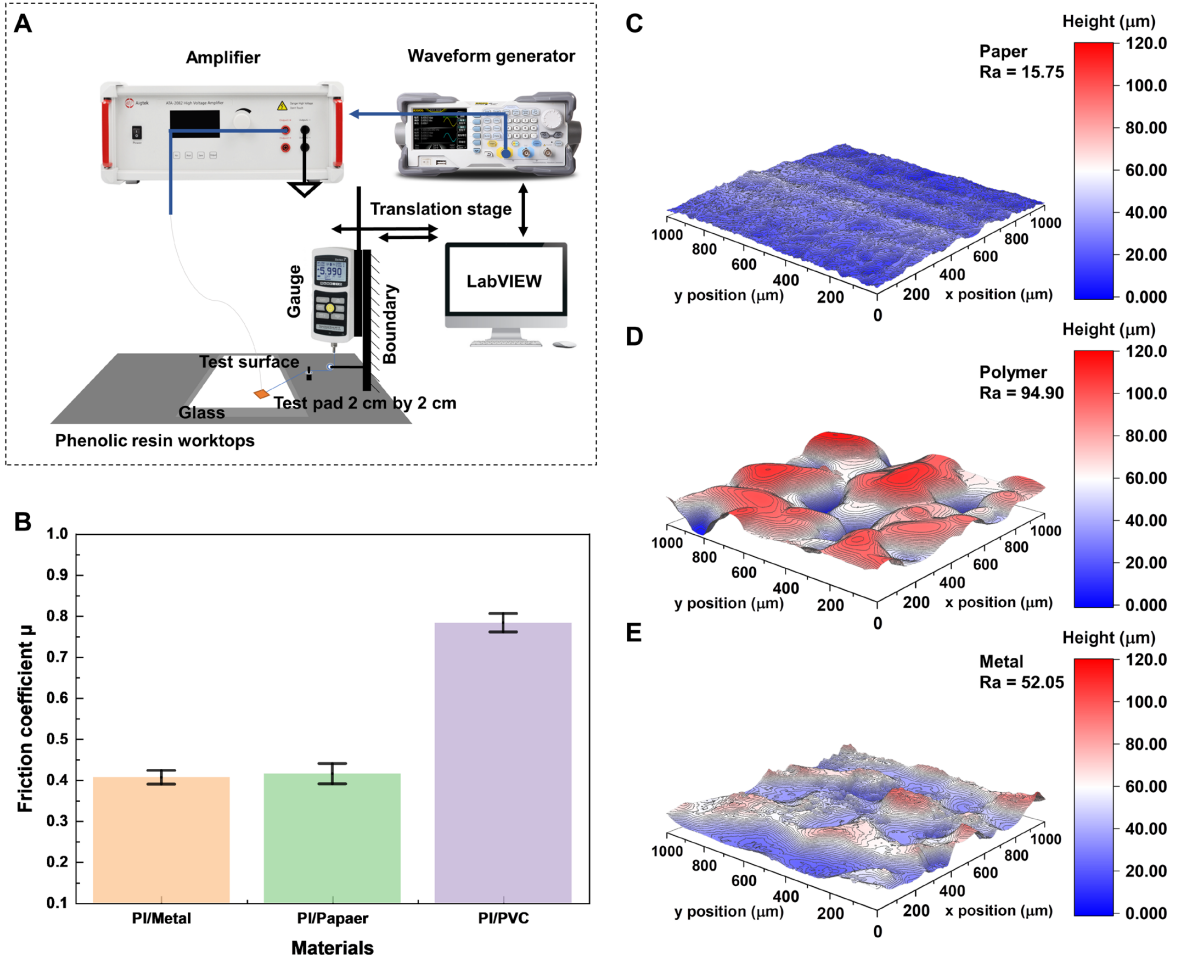


Fig. S2. Experimental setup and measuring results of the friction force. **(A)** Experimental setup for measuring the friction force. **(B)** The friction coefficient between the footpad and the ground. Surface profiles of **(C)** paper, **(D)** polymer, and **(E)** metal substrates.

Section 3: High-speed motion capture setup and basic trajectories

Fig. S3 shows the experimental setup with a highspeed camera to record the moving trajectories of the robot. The robot is placed on a substrate on top of a flat phenolic resin worktop. Two 18 μm -diameter silver wires are used to provide power to the main body of the tethered robot. A tracking camera (Powershot G7XII, Canon) is mounted on the suspension shelf on a tripod to record the moving trajectory of the robot. A highspeed camera (V710, Phantom) is placed at the edge of the testing table to record the detailed body motions of the robot. All control commands are generated in LabVIEW and a waveform generator (DG1062Z, RIGOL).

Data processing method: The moving trajectories of the robot are captured by the camera mounted on the shelf at 25 fps or 50 fps with 1080P resolution. In order to extract the trajectory data, recorded videos are processed in MATLAB with DLTdv8 from the Hedrick lab (58). We manually track the dorsal shape center of the robot frame by frame. The linear moving speed and turning radius of the robot can be calculated from the tracking data. **Fig. S4** shows various trajectory control results of the tethered prototype robot, including straight, left turn, and right turn demonstrations.

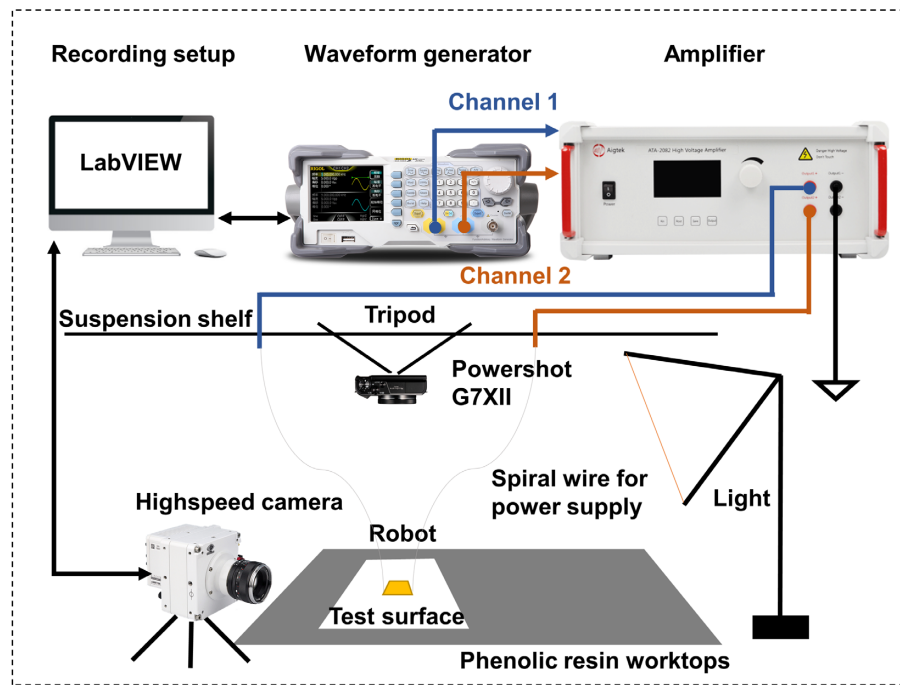


Fig. S3. Motion tracking platform. Top view motion trajectories are recorded by the Powershot G7XII camera, and the side view motion details are recorded by the highspeed camera.

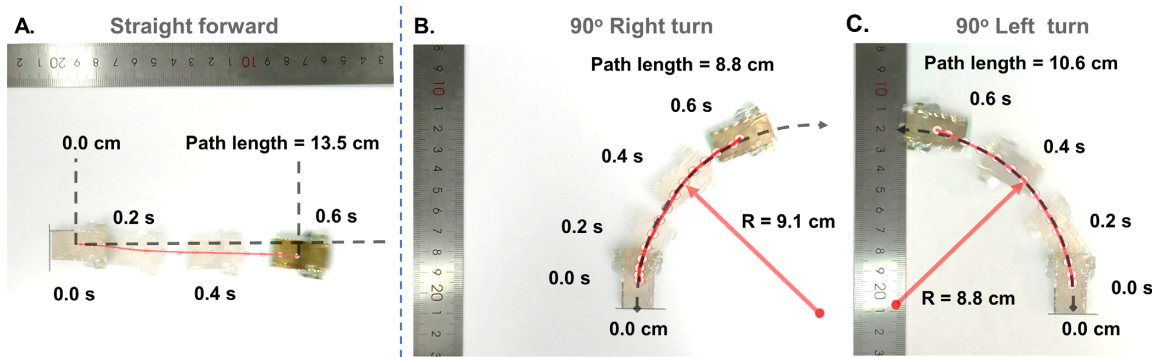


Fig. S4. Images for (A) the straight forward locomotion, and the 90-degree (B) right turn, and (C) left turn motions of a tethered robot.

Section 4. The resonant frequency of the prototype tethered robot

Table S2. The resonant frequency of different samples

Sample Number	Resonance frequency (Hz)	Weight (mg)	Structure Parameters (mm)	Load carrying
1	143 Hz	60±5 mg	$x=4, y=9.66$	No
2	163 Hz	70±5 mg	$x=4, y=9.66$	No
3	175 Hz	70±5 mg	$x=4, y=9.66$	No
4	190 Hz	70±5 mg	$x=4, y=9.66$	No
5	113 Hz	75±5 mg	$x=12.5, y=9.66$	No
6	117 Hz	75±5 mg	$x=12.5, y=5$	No
7	127 Hz	70±5 mg	$x=4, y=5$	No
8	111 Hz	260±5 mg	$x=4, y=9.66$	180 mg

Table S2 lists the resonance frequencies of different tethered robots tested in this work. Samples #1 - #4 are used in the basic characterization tests with fixed footpad positions of $x=4$ mm, $y=9.66$ mm. The resonance frequencies of these 4 samples vary from 143 Hz to 190 Hz due to minor fabrication variations and residual stresses in the legs during the folding process. Samples #5 - #7 are designed to characterize the influence of the footpad positions for the relative centripetal acceleration. These samples have some structural changes as compared with those in samples #1 - #4 to result in the reduction of resonance frequencies. Sample #8 is carrying a 180 mg payload of a commercial gas sensor to result in the reduction of the resonance frequency.

Section 5. Experimental results for left- and right-turn operations

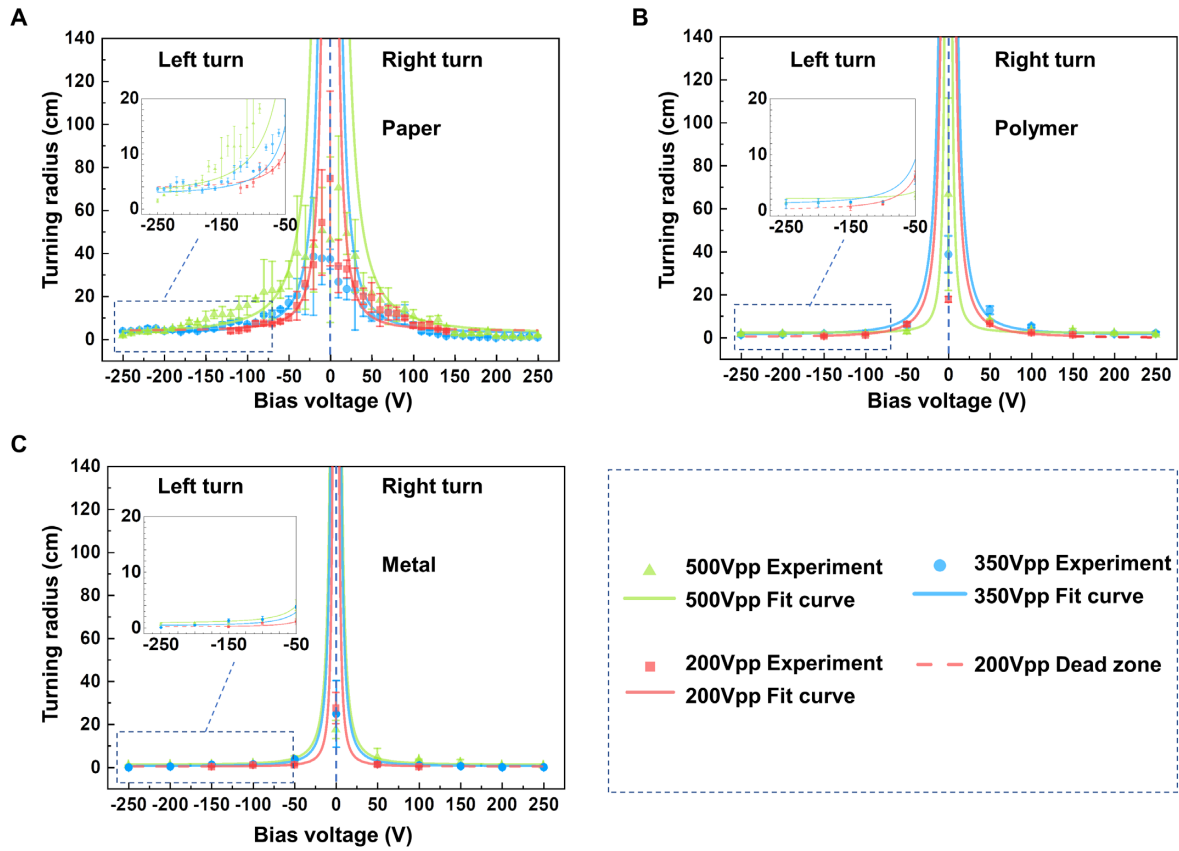


Fig. S5. Turning radius with respect to the footpad bias voltages from -250 to 250 V of a tethered robot on (A) paper, (B) polymer, and (C) metal substrates under peak-to-peak AC driving voltages of 200 V, 350 V, and 500 V.

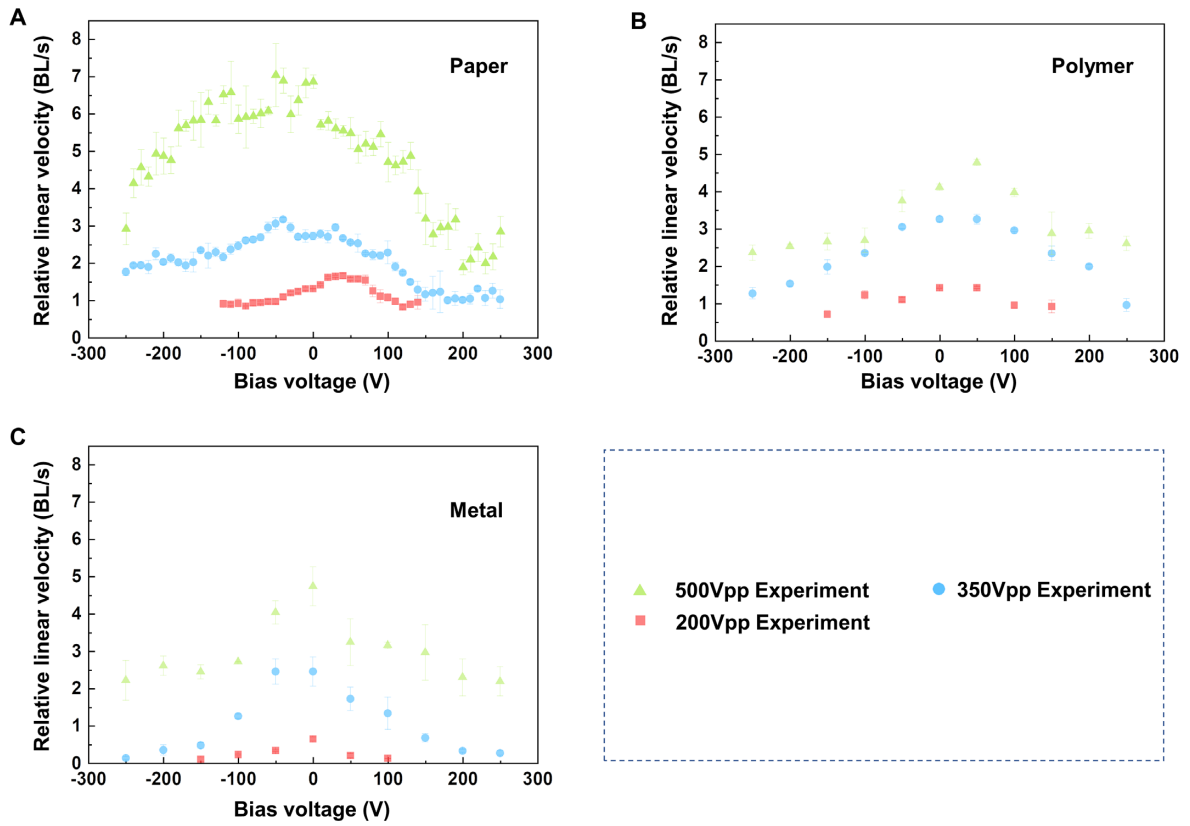


Fig. S6. Relative linear velocity with respect to the footpad bias voltages from -250 to 250 V for a tethered robot on (A) paper, (B) polymer, and (C) metal substrates, under peak-to-peak AC driving voltages of 200 V, 350 V, and 500 V.

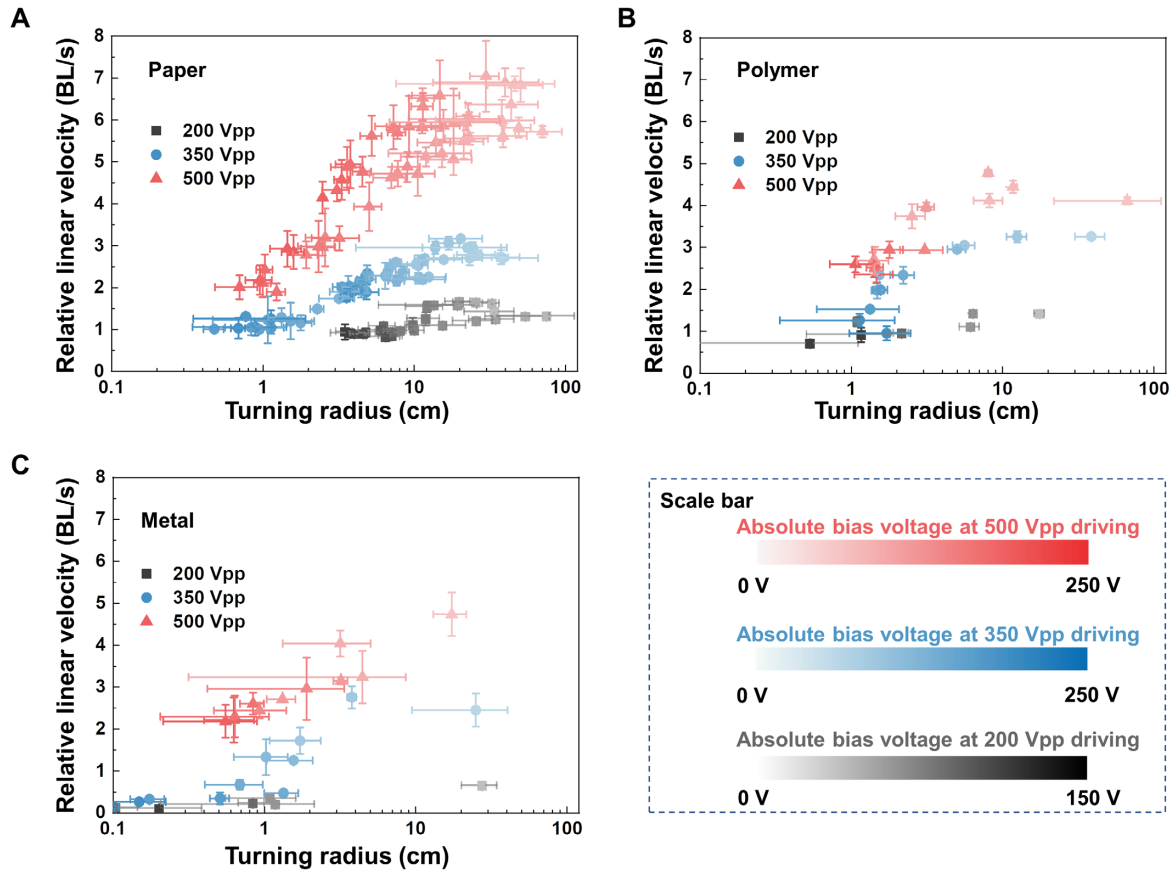


Fig. S7. Relative linear velocity with respect to turning radius under footpad bias voltages between -250 to 250 V (darker color symbols have higher absolute voltage magnitudes) for a tethered robot on (A) paper, (B) polymer, and (C) metal substrates, under peak-to-peak AC driving voltages of 200 V, 350 V, and 500 V.

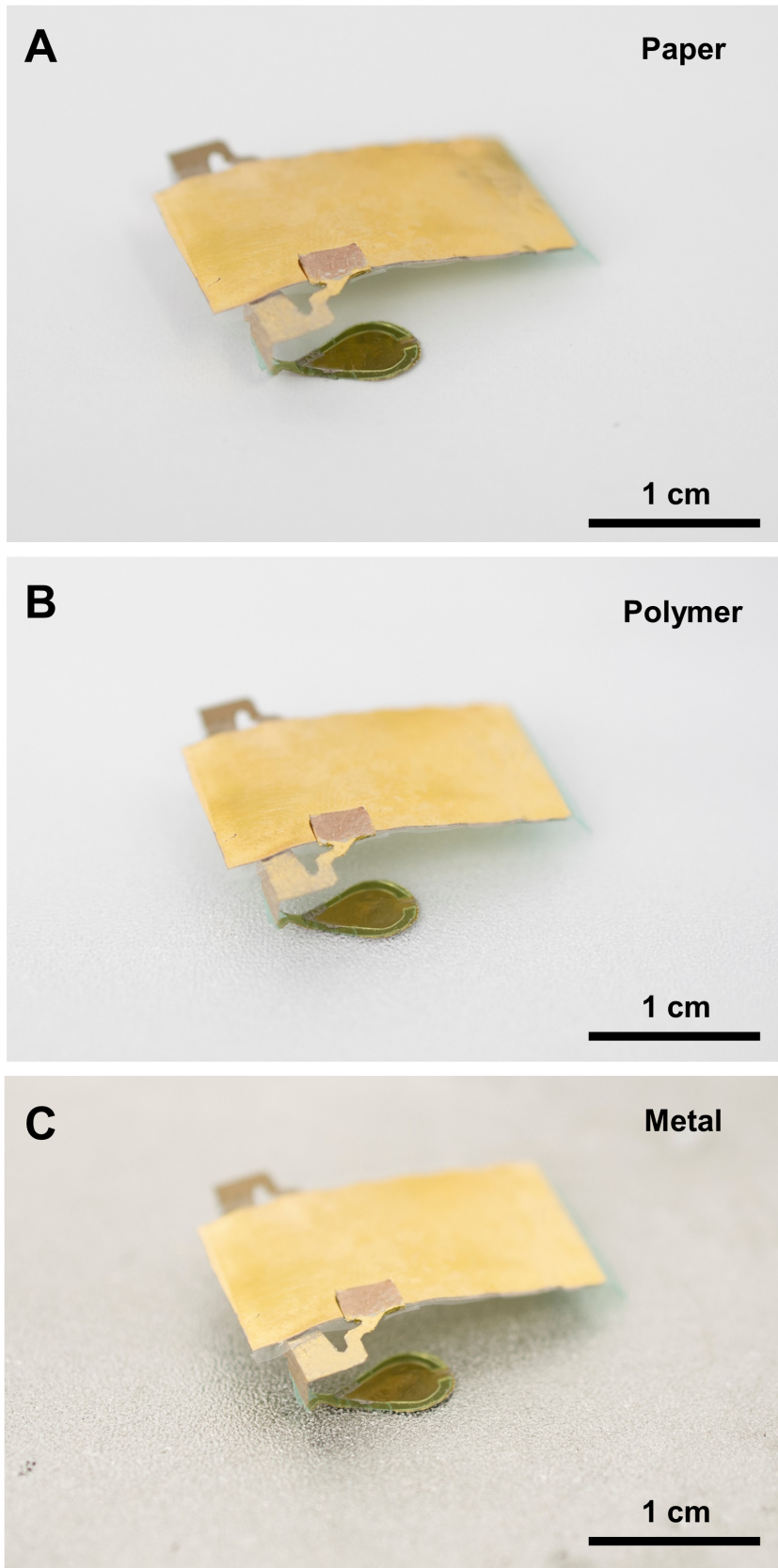


Fig. S8. Optical images showing a tethered robot on (A) paper, (B) polymer, and (C) metal substrates, respectively.

Section 6. Numerical simulation and robustness test

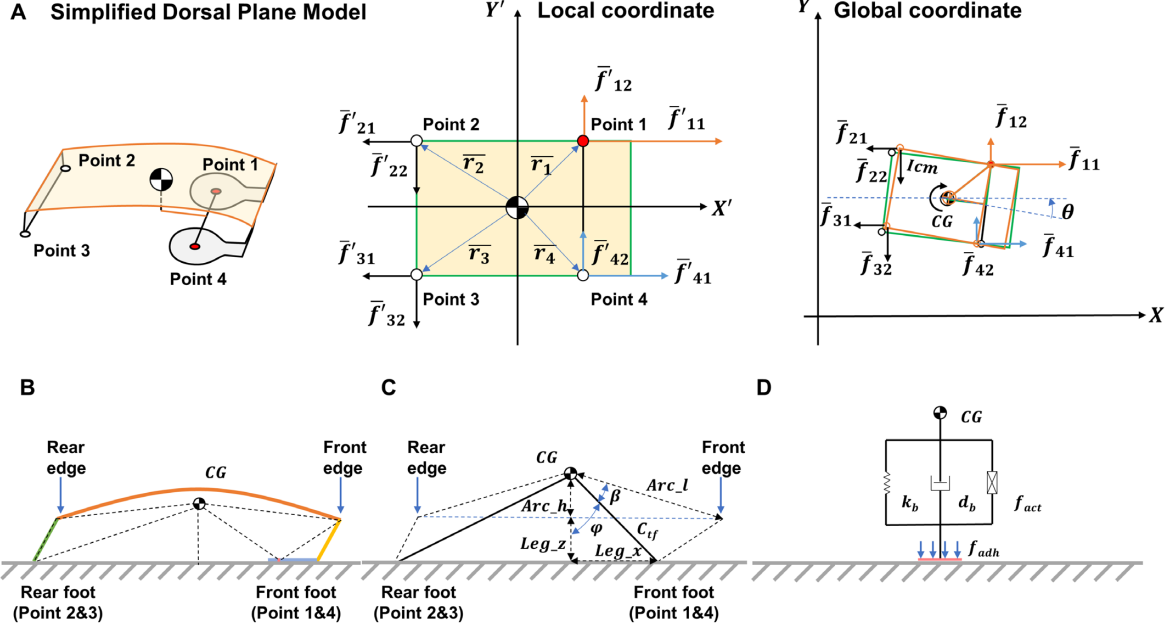


Fig. S9. Numerical simulation models. **(A)** A simplified dorsal plane model. **(B)& (C) & (D)** Normal force estimation models.

We use a simplified 4-degree of freedom (DOF) model with translation and yaw rotational motions to perform numerical simulation for our robot in MATLAB. The simplified dorsal plane model is shown in **Fig. S9A**. The body of the robot is simplified as a 2D frame from the top view. Point 1 and point 4 denote the center of the left and right front footpads, and point 2 and point 3 denote the outside points of the rear leg, respectively. Since the pitch and roll angles of the robot are very small in the real experiment, we ignore these two degrees of freedom to simplify the simulation model. The cross-sectional view of the model is shown in **Figs. S9B & C**. The dynamic model of body deformation is shown in **Fig. S9D**. We simplify the vertical body dynamics model into a spring-damper-actuator system. Since the deformation of the robot mainly occurs in the main body instead of the legs during the locomotion, we assume that the height of the leg is constant (*Leg_z*), and the original spring length is estimated to be the arch height (*Arc_h*) of the body. The spring length is an unimportant parameter compared to the stiffness, while the stiffness of the body in the model is about 1.4 ± 1 N/m measured experimentally. During the simulation, a sinusoidal wave is used as the driving signal as expressed in Eq. (5).

$$u(t) = \sin(2\pi \times freq \times t) \quad (5)$$

The acting force of the actuator has a linear relationship with the driving voltage in Eq. (6). The conversion coefficient constant, pe , can be derived from the experiment.

$$f_{\text{act}}(t) = pe \times u(t) \quad (6)$$

We use a piecewise method to simplify the model in simulation, which means two different sets of differential equations are adopted in the aerial and contact phase.

Aerial dynamics: When the foot does not touch the ground, the robot is only subjected to gravity in the vertical direction, as in Eq. (7).

$$\ddot{z} = -g \quad (7)$$

During the aerial movement, the foot is connected to the body through a spring-damper-actuator system. Hence, the acceleration of the foot can be calculated by Eq. (8).

$$\ddot{\text{foot}}z = ((kb \times (\dot{z} - \dot{\text{foot}}z) + \dot{f}_{\text{act}}) / db) + \ddot{z} \quad (8)$$

Where kb is the stiffness of the robot body, and db is the damping coefficient of the robot body. The robot is in contact with the ground when the height of the foot is equal to 0.

Contact dynamics: The speed of each point in the global coordinate system is synthesized of the speed produced by the body's extension and contraction, the linear speed brought about by the rotation, and the translational velocity of the center of gravity. The velocity of point 1 and point 4 is listed below:

$$v_i = R \begin{bmatrix} -\frac{Arc_h_t}{\sqrt{Arc_l^2 - Arc_h_t^2}} \times (1 + \frac{Leg_z}{Arc_h_t}) \times \dot{z} \\ 0 \\ 0 \end{bmatrix} + \omega \begin{bmatrix} r_{i1} \\ -r_{i2} \end{bmatrix} + v_{cg} \quad (9)$$

where the velocity of point 2 and point 3 can be estimated as:

$$v_i = R \begin{bmatrix} \frac{Arc_h_t}{\sqrt{Arc_l^2 - Arc_h_t^2}} \times \dot{z} \\ 0 \\ 0 \end{bmatrix} + \omega \begin{bmatrix} r_{i1} \\ -r_{i2} \end{bmatrix} + v_{cg} \quad (10)$$

where R is the 2D rotation matrix from the body-fixed robot frame to the world frame; ω is the angular velocity about the vertical axis; x_i and y_i are the displacements of the point i from the center of gravity (CG) in the body-fixed frame, and v_{cg} is the velocity of the CG in the world frame. The length of the arm in the x-direction, r_{i1} , can be calculated as the following:

$$r_{11} = r_{41} = \sin(\varphi) \times c_{tf} \quad (11)$$

$$r_{21} = r_{31} = -r_{11} - r_{\text{rear}} \quad (12)$$

$$\varphi = \arccos(Arc_h_t / Arc_l) - \beta \quad (13)$$

Where c_{tf} is the length from the CG to the front foot; r_{rear} is a structure constant, which defines the rear foot position; and β is a structure constant, which defines the front leg position. The force f_s acting on the CG can be calculated through the spring-damper-actuator system. The CG acceleration in the vertical direction can be calculated as:

$$f_s = (Arc_h_0 - Arc_h_t) \times kb - f_{\text{act}} - db \times \dot{z} \quad (14)$$

$$\ddot{z} = \frac{f_s}{m} - g \quad (15)$$

When the force, f_s , is greater than 0, it means that the feet are pressing down on the ground. Then the normal force of each point can be calculated as:

$$f_{1N} = \frac{f_s}{4} + \frac{1}{2} A \varepsilon_0 \varepsilon_r \left(\frac{u(t) + bias}{d} \right)^2 \quad (16)$$

$$f_{4N} = \frac{f_s}{4} + \frac{1}{2} A \varepsilon_0 \varepsilon_r \left(\frac{u(t) - bias}{d} \right)^2 \quad (17)$$

$$f_{2N} = f_{3N} = \frac{f_s}{4} \quad (18)$$

If the force, f_s , is less than 0, it means that the feet are pulling off the ground. Then the normal force of each point should be calculated as:

$$f_{1N} = \frac{f_s}{2} + \frac{1}{2} A \varepsilon_0 \varepsilon_r \left(\frac{u(t) + bias}{d} \right)^2 \quad (19)$$

$$f_{4N} = \frac{f_s}{2} + \frac{1}{2} A \varepsilon_0 \varepsilon_r \left(\frac{u(t) - bias}{d} \right)^2 \quad (20)$$

$$f_{2N} = f_{3N} = 0 \quad (21)$$

Since the rear feet have no electrostatic adhesion force, the force between the rear feet and the ground at this time becomes 0. If the total force of the feet is less than 0, the robot separates from the ground. The friction force of each point is derived from Eq. (22). The friction coefficient of the footpads and rear legs in the simulation is derived from the experiment in **Fig. S2B**.

$$\bar{f}_i = -f_{IN}(\mu_d + (\mu_s - \mu_d)e^{-\left(\frac{|\bar{v}_i|}{v_s}\right)^p}) \tanh(k_t v_s) \begin{bmatrix} \frac{v_{i1}}{|\bar{v}_i|} \\ \frac{v_{i2}}{|\bar{v}_i|} \\ 0 \end{bmatrix} \quad (22)$$

The rotational motion of the robot under the local coordinate can be calculated from Eq. (23).

$$T = \sum_{i=1}^4 \bar{r}_i \times (R \bar{f}_i) \quad (23)$$

where R is the rotation matrix to convert the global coordinate to the local coordinate system. Finally, the dynamic matrix is constructed as below.

$$\begin{bmatrix} m & & & \ddot{x} \\ & m & & \ddot{y} \\ & & m & \ddot{z} \\ & & & I_{cm} \end{bmatrix} \begin{bmatrix} \ddot{x} \\ \ddot{y} \\ \ddot{z} \\ \ddot{\theta} \end{bmatrix} = \begin{bmatrix} \sum f_{i1}' \\ \sum f_{i2}' \\ f_s/m - g \\ T \end{bmatrix} \quad (24)$$

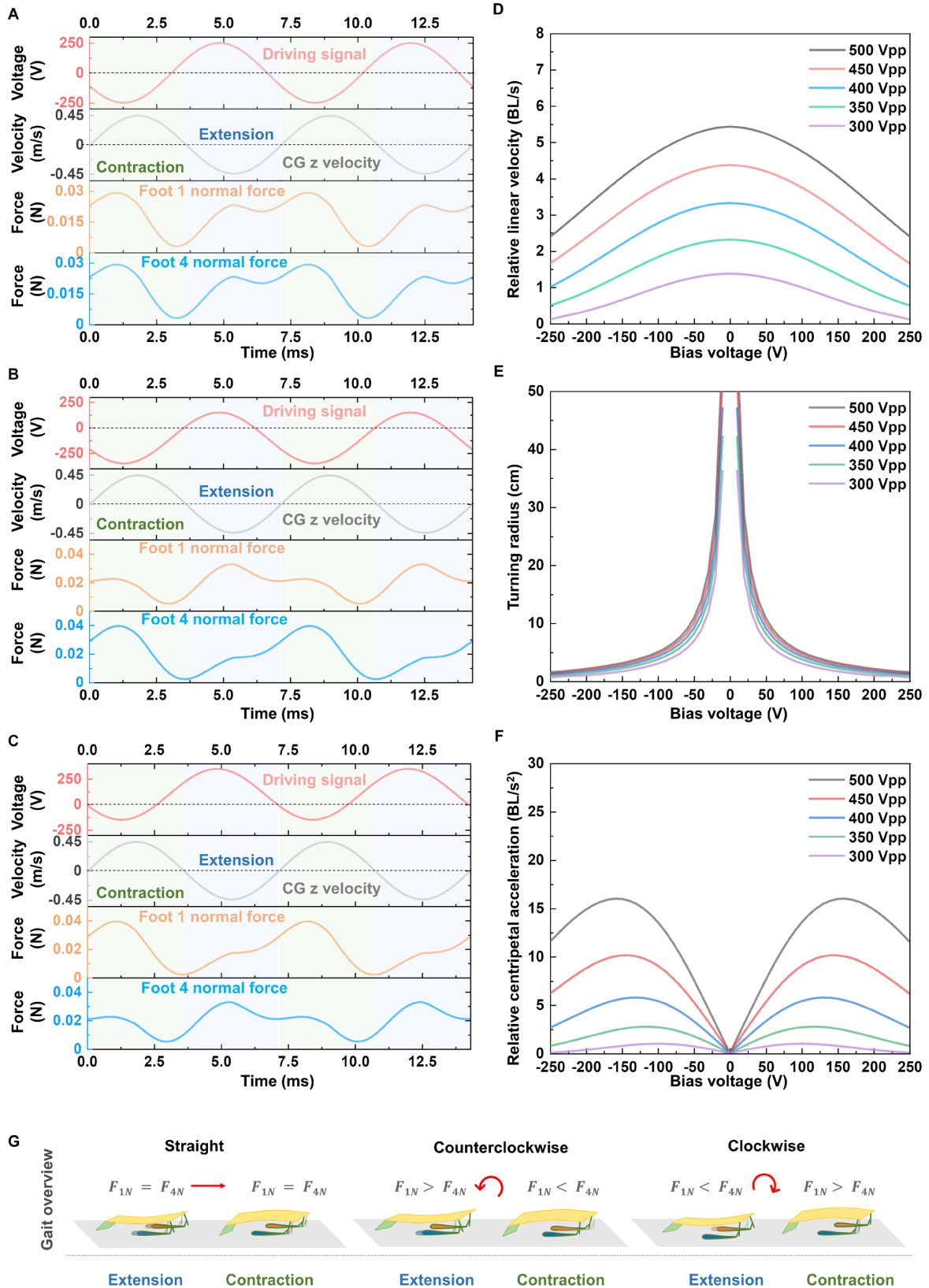


Fig. S10. Numerical simulation results. **(A) & (B) & (C)** Driving signal, moving velocity and force distributions during the forward motion, left turn, and right turn, respectively. **(D)** Relative linear velocity

with respect to bias voltage. **(E)** Turning radius with respect to bias voltage. **(F)** Relative centripetal acceleration with respect to bias voltage. **(G)** Gait overview for straight forward motion, left turn, and right turn, respectively.

Straight forward movement: During the straight forward movement, there is no bias-voltage applied with the driving signal, as shown in the first row of **Fig. S10A**. The main body motion state can infer from the CG vertical movement speed. If the velocity of the CG vertical movement is larger than 0, the main body is contracting. Otherwise, the main body is extending. The force distributions of the left foot #1 and the right foot #4 are shown in the third and fourth row in **Fig. S10A** with the corresponding gait overview in **Fig. S10G**. Obviously, without the bias voltage, the normal force of the left foot #1 and the right foot #4 are equal. Therefore, no steering torque is generated. On the other hand, the average value of the normal force of the foot in the contraction phase is slightly larger than that in the extension phase. This means that the robot's forward driving efficacy is greater than the driving efficacy for the backward movement, which is the main reason for the robot's forward movement.

Left turn: When a negative bias voltage is applied, the normal force distribution of left foot #1 and the right foot #4 becomes unequal, as shown in **Fig. S10B**. During the contraction phase of the main body, the normal force on the right foot #4 is greater than the normal force on the left foot #1. A counterclockwise torque is generated due to the inequivalent friction force in the contraction phase. In contrast, the normal force on the left foot #1 becomes larger than the normal force on the right foot #4 in the extension period. Also, a counterclockwise torque is generated while the robot is in the extending period. In summary, when a negative bias voltage is applied, the inequivalent forces on the left foot #1 and the right foot #4 will generate the counterclockwise torque, which leads to the counterclockwise turn of the robot.

Right turn: If a positive bias voltage is applied, as shown in **Fig. S10C**, the force distribution becomes reversed when compared to the force distribution when the negative bias voltage is applied. Therefore, a clockwise torque is generated by the left foot #1 and the right foot #4 during the movement, which leads to the clockwise turn of the robot.

Speed variation: The speed variation result is shown in **Fig. S10D**. Obviously, the speed is affected by the driving voltage as a larger driving voltage provides a larger contraction and extension deformation of the main body, which leads to faster linear moving speeds. Besides, the moving speed is also influenced by the bias voltage. If the bias voltage increases, the adhesion force during the extension also increases, and it leads to the increase of the resistance force during the forward motion. Therefore, as the bias voltage increases, the linear moving speed of the robot decreases.

Turning radius variation: The turning radius variation result is shown in **Fig. S10E**. If the absolute value of the bias voltage increases, the normal force difference between the left foot #1 and right foot #4 also increases. This results in an increase in the torque and leads to a decrease in the turning radius.

Relative centripetal acceleration variation: The relative centripetal acceleration variation is shown in **Fig. S10F**. The lateral acceleration of the robot is calculated from both the speed and turning radius through the Eq. (25).

$$a_r = \frac{V^2}{R_{\text{turn}}} \frac{1}{BL} \quad (25)$$

where V and R_{turn} are the turning speed and turning radius, and BL is the body length of the robot. The agility of the robot is affected by both the driving voltage and the bias voltage. As the bias voltage increases, the steering torque increases to results in a smaller turning radius. However, this will also reduce the linear velocity due to the increase of adhesion force to the ground. Therefore, under the same AC driving voltage, the relative centripetal acceleration of the robot may reach a maximum value at moderate bias voltage values. In this case, the robot has the best agility. Furthermore, a higher driving AC voltage leads to faster linear velocities to increase agility.

Comparison between the simulation and experimental results: The direct comparison of experimental and simulation results is shown in **Fig. S11** to validate the trend for (1) the radius (R) of the turning motion, (2) the relative linear velocity (V), and (3) the relative centripetal acceleration of the robots *versus* the applied footpad bias voltages under a 500 Vpp driving voltage. It is noted that a 500 Vpp square-wave shape voltage source has been applied in experiments, while a 500 Vpp sinusoidal-wave voltage has been used in simulations because simulations won't converge by using the square-wave inputs. Intuitively, under the same

magnitude, the square-wave inputs provide more energy into the system as compare that of the sinusoidal-wave inputs to result in a larger striking force, which results in slightly higher linear velocities and radii in turning motions in experiments as compared to those in simulations. The relative centripetal acceleration is proportional to both parameters with a relationship of V^2/R in Eq. (25), while the simulation results can predict this general trend.

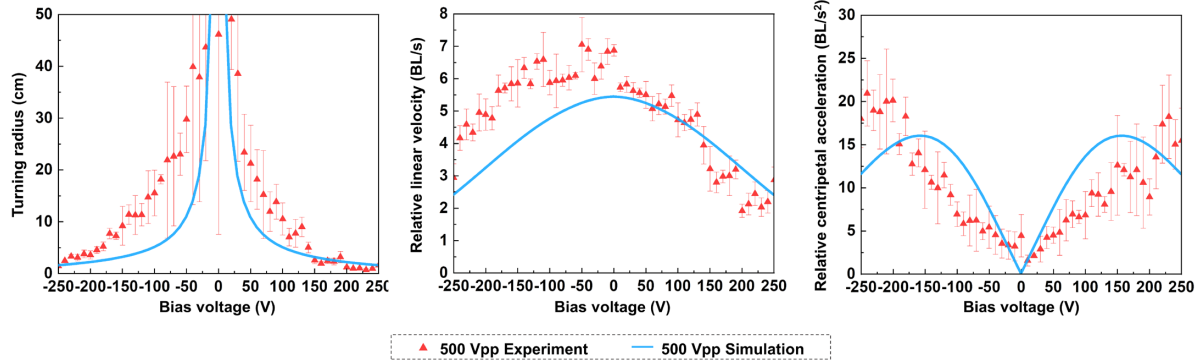


Fig. S11. Experiment and simulation results for the radius of the turning motion, relative linear velocity, and relative centripetal acceleration versus the applied footpad bias voltage under a 500 Vpp driving voltage.

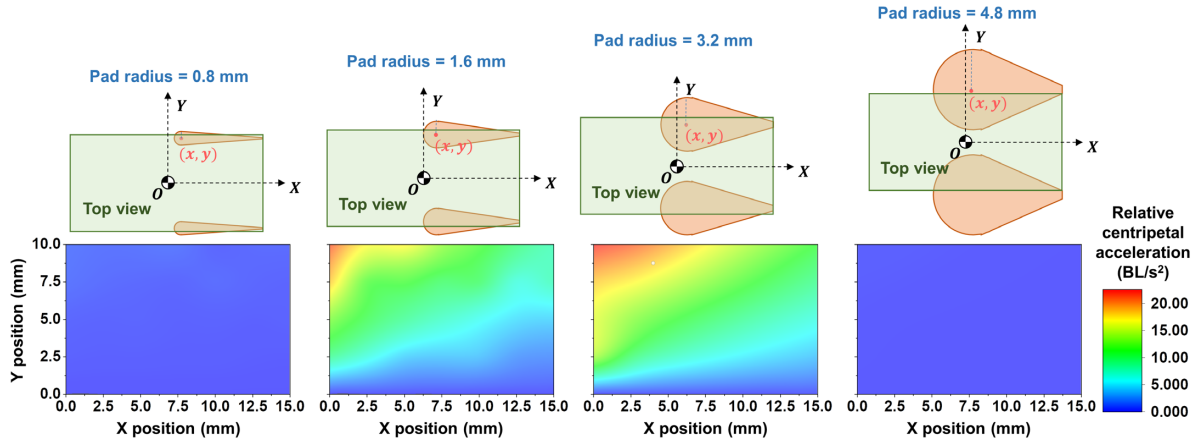


Fig. S12. Simulation results for the relative centripetal acceleration of the robot with different footpad sizes (radius = 0.8, 1.6, 3.2, and 4.8 mm).

The agility of the robot is affected by the position of the footpads and is also influenced by the footpad size. As shown in Eqs. (16, 17, 19, 20), the electrostatic force is linearly proportional to the footpad contact area. Numerical simulations in MATLAB based on different footpad sizes are conducted with the results shown in **Fig. S12**. The large footpad size results in a large contact area and large electrostatic attraction force.

However, as the electrostatic adhesion force increases, the linear speed of the robot decreases, as discussed before. Hence, the relative centripetal acceleration decreases as shown if the footpad size radius is too big (such as larger than 4.8 mm). On the other hand, the electrostatic force decreases as the size of the footpad decreases. A small footpad radius (such as below 0.8 mm) may generate insufficient steering torque to steer the robot such that the relative centripetal acceleration also reduces, as shown in **Fig. S12**. In summary, the appropriate footpad size is important to achieve the high relatively centripetal acceleration.

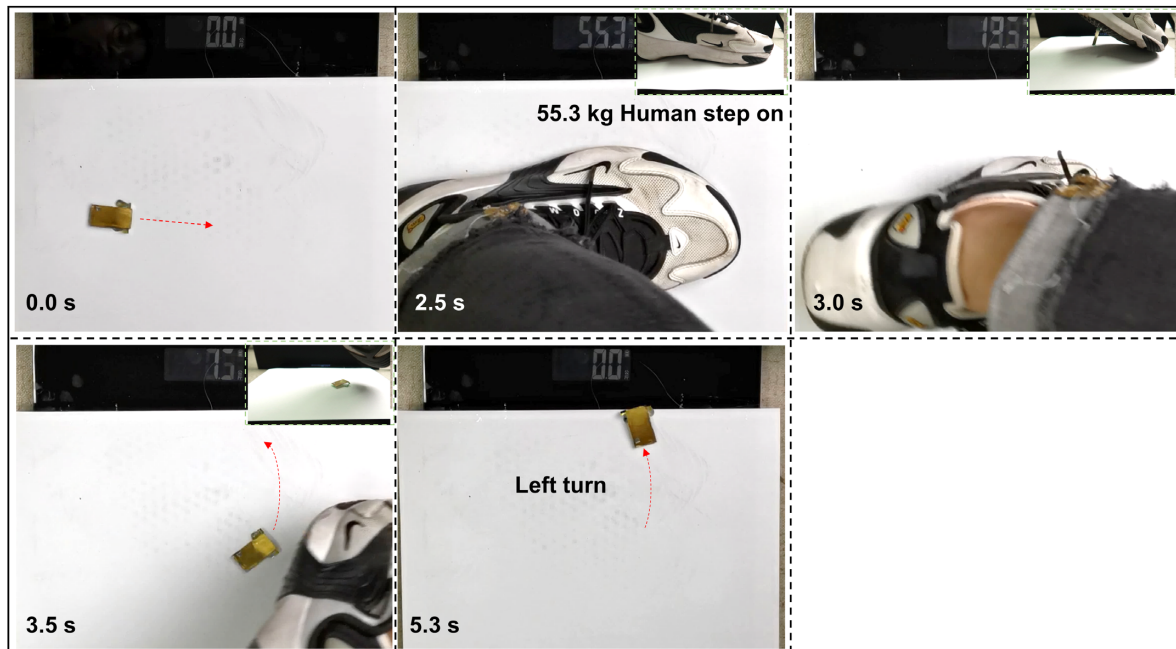


Fig. S13. Robustness test for the robot by stepping on it from a volunteer with a weight of 55.3 kg. The robot keeps good turning/running capability afterward to show good robustness.

Section 7. Gas detection platform

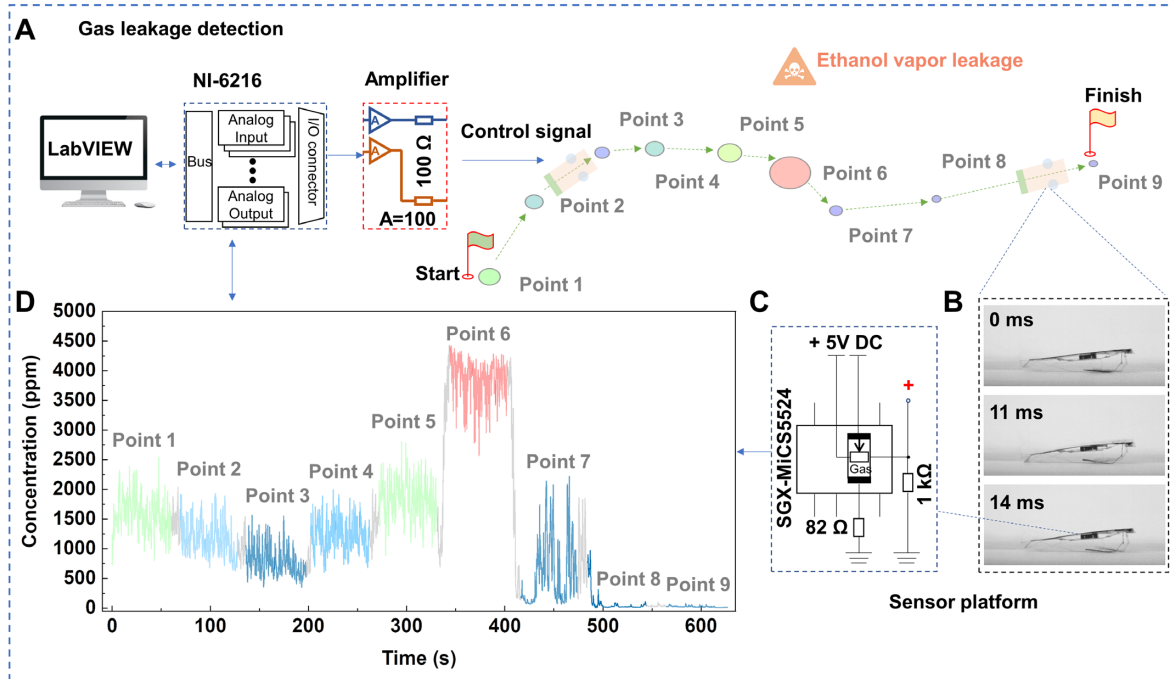


Fig. S14. The experimental setup and details for the gas detection demonstration. **(A)** The experimental setup and moving path for the gas leakage detection demo. **(B)** Cross-sectional view images of a robot with the gas sensor in the initial (0 ms), extending (11 ms), and contracting (14 ms) states. **(C)** The gas sensor electrical connections. **(D)** Detected ethanol gas concentration at 9 points with respect to time.

The gas detection platform consists of a computer, a multifunction DAQ device (6216-USB, NI), an amplifier (ATA-2082, Agitek), and a commercial MEMS gas sensor (MiCS5524, SGX, T90 with the response time of less than 10 s), as shown in **Fig. S14**. The gas sensor is calibrated before usage. To simulate a gas pipe leaking situation, a 48 mm in diameter tube is constructed by Lego bricks (Lego Inc.), and one end is sealed. A fan is placed at the other end of the LEGO pipe, and a small hole on the pipe (the blue brick) is designed to leak the alcohol gas. A flexible holder made of PET is connected to the bottom of the main robot body through the silicon adhesion layer, and the sensor is mounted on the holder *via* the adhesion layer. The gas sensor signals are acquired through the DAQ device in real-time. The robot's motion control signals are adjusted for the tethered robot to pass a designed sensing route as shown and stop for 60 seconds at each of the 9 spots to record the gas concentration route map to identify the gas leakage location.

Section 8. Design of the untethered soft robot

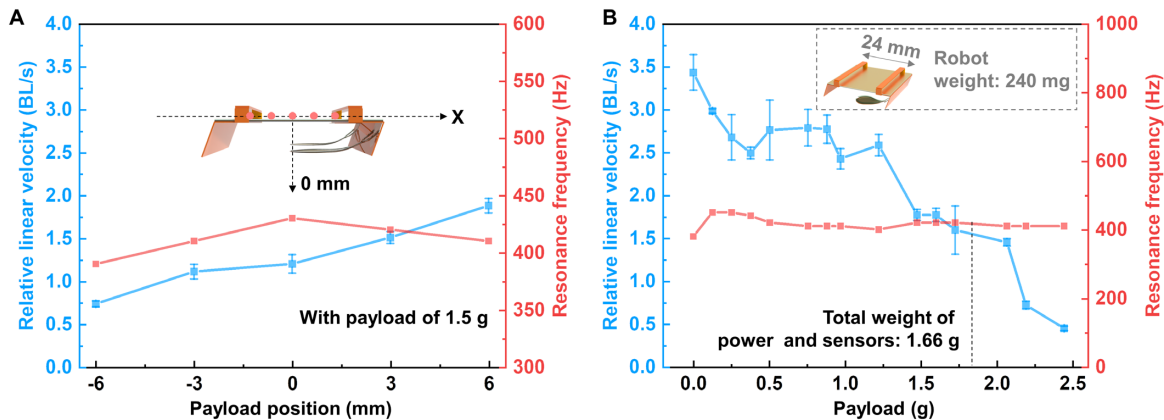


Fig. S15. Payload test of the untethered robot with a different design. **(A)** The linear moving velocity tested at the resonant frequency of the untethered robot design (240 mg) with a payload of 1.5 g on the top robot body *versus* the payload position. **(B)** Linear velocity and resonance frequency versus the payloads of 0 to 2.5 g for the untethered robot.

The body size of the untethered robot is $24 \times 22 \text{ mm}^2$, which is about 17.3% larger than that of the tethered robot at $30 \times 15 \text{ mm}^2$. However, to support the heavy payload (electronics and battery), two supporting frames and an extra front supporting structure made of 200 μm -thick PI films are added. Specifically, the front supporting structure is $8 \times 22 \times 0.2 \text{ mm}^3$ and a single supporting frame is $2 \times 50 \times 0.2 \text{ mm}^3$ (after the folding process, the frame forms a 3D hollow structure of $2 \times 22 \times 2 \text{ mm}^3$ to support the large payload). As such, the total area of the additional components is about 71.2% of the body size of the tethered robot. However, these new components using the 200 μm -thick PI layer (with a 25 μm -thick silicone adhesion layer) are about 3.3 times thicker than the original robot body made of mainly 18 μm -thick PVDF and 25 μm -thick PET (with a 25 μm silicone adhesion layer) to result in a total of 2.7 times (175 mg) additional weight than that of the tethered robot. The linear moving velocities tested at the resonant frequency of the untethered robot (240 mg) with a payload of 1.5 g on the top robot body *versus* the payload position are shown in **Fig. S15A**. The five positions are measured from the center of the robot at an interval of 3 mm. It is found that payload mounted at the center position may have induced a slightly larger deformation (stress) on the robot body to induce a higher resonant frequency. Furthermore, the measured linear moving velocity increases as the payload is placed closer to the head position, which is the key region to induce the forward movements from the two front-pads. On the other hand, the linear moving velocity and resonance frequency *versus* the payloads of 0 to 2.5 g are shown in **Fig. S15B**. The payload is mounted 6 mm from the center of the robot

and close to the head location. The linear velocity decreases as the payload increases as expected. The prototype robot without any payload has a linear velocity of 3.4 BL/s, and the velocity decreases to 0.4 BL/s with a 2.5 g (10.4 times body weight) payload. The untethered robot integrated with a battery, two photoresistors and a flexible circuitry for a total payload of 1.66 gram has a linear velocity of 1.2 BL/s (for a short-term operation). On the other hand, the resonance frequencies for the untethered robot with payloads from 0 to 2.5 grams have been characterized to be between 380 to 420 Hz.

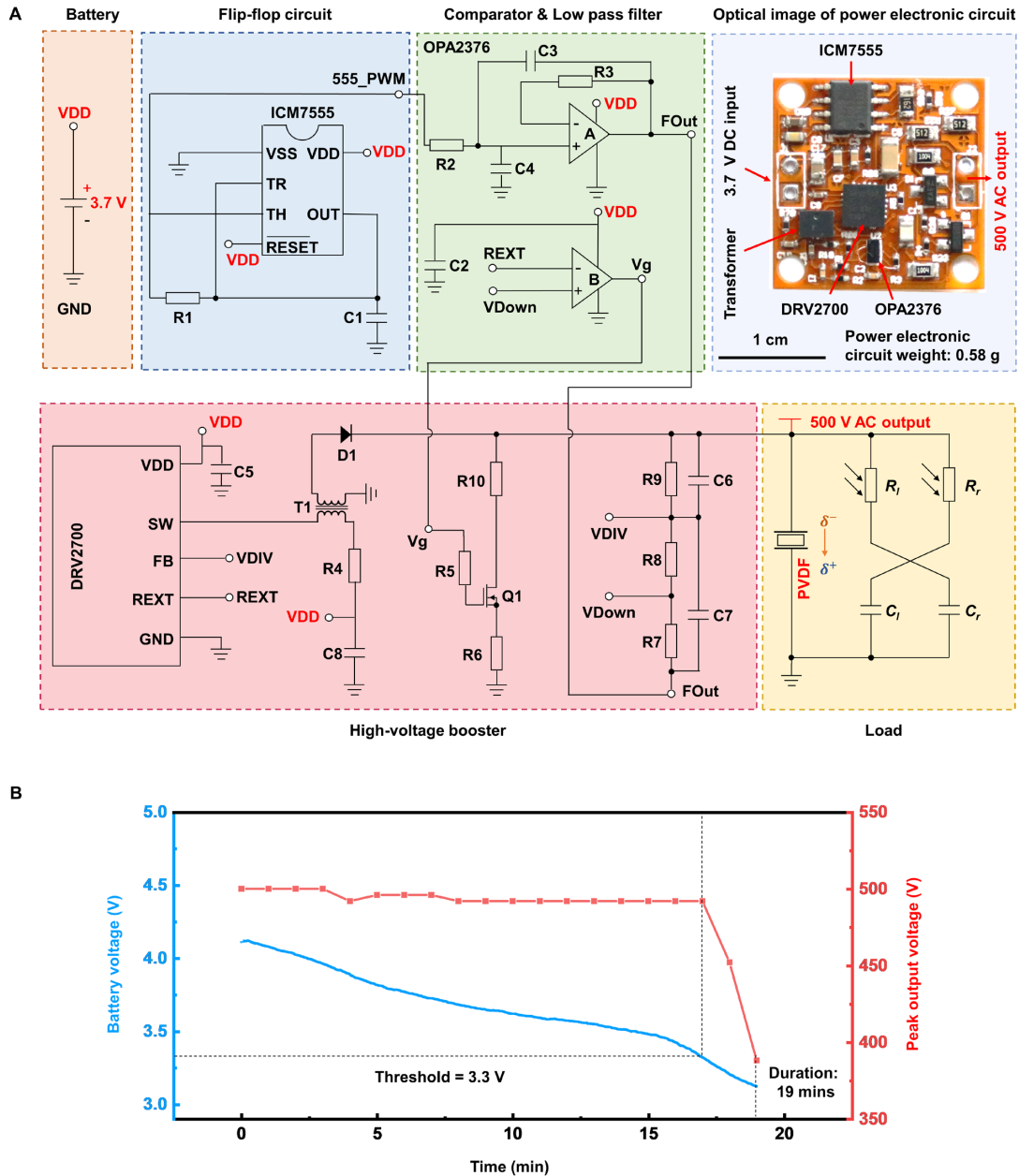


Fig. S16. The power electronics circuit and endurance test of the untethered robot. **(A)** The power electronic circuit and an optical image. **(B)** Endurance test results by monitoring the battery voltage (blue) and peak output voltage (red) of the untethered robot.

The untethered power electronic circuit, powered by a Li-polymer battery (3.7 V standard voltage, 40 mAh, HuiXinLi, Inc.), can generate a square wave with a frequency of 410 Hz and amplitude around 500 V. The circuit has three key subcomponents: the flip-flop circuit, low-pass filter, and high-voltage booster as shown in **Fig. S16A**. The detailed component parameters and weight are shown in **Table S3**. A 555 timer (ICM7555, Intersil Inc.) is utilized to build a flip-flop circuit to generate the 410 Hz square wave signal. The signal is then sent to a high-voltage flyback converter chip (DRV2700, Texas Instrument Inc.) through a low pass filter. A comparator is used to operate the pulldown network to decrease the discharge time. The endurance test results of the untethered robot are shown in **Fig. S16B**. The output voltage of the circuit can sustain around 500 V when the battery voltage is over the threshold of 3.3 V. With the supply voltage below the threshold, the peak voltage of the output waveform will have a rapid drop. The untethered robot equipped with a 40 mAh battery has an operation time of 19 minutes and a moving distance of 31 meters.

Table S3. Components of the untethered power electronic circuit

Component	Notation	Parameter	Package	Weight (mg)
Capacitor	C1, C5, C9	1 μ F, 0.1 μ F, 0.1 μ F	0603	21
	C2, C3, C4, C7	0.1 μ F, 3.9 nF, 1 nF, 8.2 nF	0402	6
	C6	22 pF	0805	17
Resistor	R1, R9, R10	1.6 k Ω , 1M Ω , 5.1 k Ω	0805	15
	R2, R3, R4, R5, R6, R7, R8	49.9, 10, 0, 10, 0.22, 5.1, 0.392 k Ω	0402	4
Timer	U1	ICM 7555	SOP-8	82
Operational amplifier	U2	OPA 2376	WCSP-8	5
Power management	U3	DRV 2700	VQFN-20	47
MOSFET	Q1	BSS127 H6327XTSA2	SOT-23	11
Diode	D1	MMBD3004S-7-F	SOT-23	12
Transformer	T1	ATB322515-0110	SMT	80
FPCB		L: 20 mm; W: 20 mm; T: 200 μ m		120
Solder				~160
Power electronic circuit weight: 580 mg				
Photoresistor sensors	R _l , R _r	GL3549	RAD-0.2	220
Lithium Battery		40 mAh	521012	860
Sensors and battery weight: 1080 mg				
Total Weight:				1660

The cost of transport (COT) of the untethered robot is calculated from the measured battery power consumption data by the charge/discharge cycling equipment (S400, MACCOR Inc.) during the endurance test for 19 minutes. The average power is 397 mW and the average moving speed of the untethered robot (without sensor) is 27.2 mm/s.

$$COT = \frac{P}{mgv} = \frac{397 \times 10^{-3} \text{ W}}{1.68 \times 10^{-3} \text{ kg} \times 9.8 \text{ m/s}^2 \times 0.0272 \text{ m/s}} = 887 \quad (26)$$

The electromechanical conversion efficiency of an actuator can be defined as the ratio of mechanical output energy (including the kinetic and elastic energy) to the electrical input energy in one cycle. In this work, the total mechanical output energy is calculated at the resonance frequency of the actuator using the deformation profile captured by a high-speed camera. The electromechanical conversion efficiency is estimated as 15.3%, which is within the range in the datasheet provided by the PVDF film vendor. The driving electrical circuit efficiency, η_c , can be calculated as:

$$\eta_c = \frac{E_o}{E_i} = \frac{\int_0^t \frac{U_o^2}{R} dt}{U_i I_i t} \quad (27)$$

where E_o and E_i are the output and input energy, respectively; U_o is the electrical output voltage; R is the resistance of the load resistor; t is the time period; U_i is the input voltage; and I_i is the input current. Using a load resistor of 2 MΩ, the driving circuit efficiency is measured as 11.8% at 400 Hz. The driving circuit efficiency of a previously reported insect-scale untethered robot is 7.5% when the load resistor is 2 MΩ (20).

Section 9. Figure of merit data

Table S4. Figure of merit data

Species	Linear velocity (mm/s)	Turning radius (mm)	Angular velocity (°/s)	Body length (m)	Centripetal acceleration (m/s ²)	Relative centripetal acceleration (BL/s ²)	Ref.
Mammal							
Cheetah	-	-	-	1.05	12.96	12.34	(29)
Impala	-	-	-	1.02	11.13	10.91	(29)

Dielectric elastomer	-	6	62.79	0.085	0.00719	0.08	(19)
Dielectric elastomer	-	6	30	0.040	0.00164	0.04	(20)
Dielectric elastomer	-	28.5	14.53	0.1	0.00183	0.02	(21)
Pneumatic	0.28	6.4	-	0.21	1.23e-5	5.83e-5	(14)
Pneumatic	5	1500	-	0.65	1.67e-5	2.56e-5	(15)
Pneumatic	1.68	43.04	-	0.23	6.56e-5	0.000285	(16)
Pneumatic	15	38.2	-	0.1	0.00589	0.06	(17)
Piezoelectric	60	-	108.06	0.03	0.11	3.77	(48)
Nylon	2.39	109.76	-	0.055	5.20e-5	0.000946	(49)
DC motor	22.88	16.67	-	0.44	0.03	0.07	(50)
This work (paper)	139	28	-	0.03	0.69	23	
This work (polymer)	109	21	-	0.03	0.57	19	
This work (metal)	108	14	-	0.03	0.84	28	